communications materials

ARTICLE

https://doi.org/10.1038/s43246-022-00254-2 OPEN

Single thermodynamic transition at 2 K in superconducting UTe_2 single crystals

Priscila F. S. Rosa [1✉], Ashley Weiland[1], Shannon S. Fender[1], Brian L. Scott [1], Filip Ronning[1], Joe D. Thompson[1], Eric D. Bauer [1] & Sean M. Thomas [1]

UTe_2 is a newly-discovered unconventional superconductor wherein multicomponent topological superconductivity is anticipated based on the presence of two superconducting transitions and time-reversal symmetry breaking in the superconducting state. The observation of two superconducting transitions, however, remains controversial. Here we demonstrate that UTe_2 single crystals displaying an optimal superconducting transition temperature at 2 K exhibit a single transition and remarkably high quality supported by their large residual resistance ratio and small residual heat capacity in the superconducting state. Our results shed light on the intrinsic superconducting properties of UTe_2 and bring into question whether UTe_2 is a multicomponent superconductor at ambient pressure.

[1] Los Alamos National Laboratory, Los Alamos, NM 87545, USA. ✉email: pfsrosa@lanl.gov

Uranium is a fascinating element located at the border between localized and delocalized 5*f* wavefunctions. Uranium-based materials may therefore be found close to a magnetic-nonmagnetic boundary at which unconventional superconductivity is generally expected to emerge. According to the Hill limit, superconductivity is favored when the distance between uranium atoms, d_{U-U}, is smaller than 3.6 Å, whereas localized wavefunctions favor magnetic order when $d_{U-U} > 3.6$ Å[1,2]. Unconventional actinide superconductors, however, remain a rather sparse class of strongly correlated materials that host many puzzling emergent properties. Hidden order in tetragonal URu_2Si_2[3,4], time-reversal symmetry breaking in the superconducting state of hexagonal UPt_3[5,6], and contradicting reports on whether cubic UBe_{13} is a spin-singlet or a spin-triplet superconductor[7–9] are just a few examples. Other prominent examples include hexagonal antiferromagnetic UM_2Al_3 (M = Ni, Pd)[10,11] and orthorhombic ferromagnetic superconductors UGe_2, UCoGe, and URhGe[12,13].

In 2019, orthorhombic UTe_2 became a new member of this family [14]. Early reports observed a superconducting transition at $T_c = 1.6$ K and a remarkably large upper critical field exceeding 40 T, a value much higher than the expected Pauli limit for a spin-singlet state[14–17]. Nuclear magnetic resonance (NMR) measurements found that the decrease in Knight shift below T_c is much smaller than the expectation from spin-singlet pairing[18]. Though no magnetic order is observed above 25 mK *via* muon spin resonance measurements[19], *a*-axis magnetization data can be described by the Belitz-Kirkpatrick-Votja theory for metallic ferromagnetic quantum criticality[14]. UTe_2 was therefore proposed to be close to a ferromagnetic quantum critical point akin to UGe_2, UCoGe, and URhGe[13]. The shortest U-U distance in UTe_2 within the *c*-axis dimers, 3.8 Å, supports proximity to a magnetic instability, but inelastic neutron scattering measurements as well as pressure- and field-dependent thermodynamic properties point to dominant antiferromagnetic fluctuations[20–25].

The orthorhombic crystal structure of UTe_2 implies that all irreducible point group representations are one-dimensional. If time-reversal symmetry is broken below T_c, the superconducting order parameter is thus required to contain two (one-dimensional) components with a relative phase between them[26]. Recently, the presence of two transitions in specific heat data combined with time-reversal symmetry breaking probed by the polar Kerr effect support the presence of a multicomponent superconducting order parameter in UTe_2. Kerr trainability along the *c* axis and symmetry requirements in the D_{2h} point group further indicate that the two superconducting order parameters belong to a combination of either B_{3u} and B_{2u} or B_{1u} and A_u spin-triplet channels. In this case, UTe_2 is a topological superconductor with Weyl nodes and surface Fermi arc states[26].

The observation of two superconducting transitions in UTe_2, however, remains disputed as independent groups observe a single transition and evidence for inhomogeneity in double-transition samples[16,27–29]. The superconducting properties of UTe_2 are strongly dependent on the synthesis route, which further highlights the crucial role of sample quality in determining the intrinsic properties of unconventional superconductors. UTe_2 crystals grown by the self-flux method show no signs of bulk superconductivity, whereas crystals grown by chemical vapor transport show either a split transition or a single transition[16]. Notably, specific heat data show an apparent lack of entropy conservation between the superconducting and normal states, and a large residual Sommerfeld coefficient of unknown origin is observed in the superconducting state, γ_{SC}. Further, the highest reported T_c of 1.77 K yields a single transition and an inverse correlation between T_c and γ_{SC}[27,30]. Key outstanding questions are therefore whether the optimal T_c in UTe_2 leads to entropy conservation and how the purported multicomponent transition responds to changes in T_c.

Here we show that UTe_2 crystals with the highest superconducting transition temperature, $T_c = 2$ K, exhibit a single thermodynamic transition. The high quality of the crystals is demonstrated by their high residual resistance ratio, RRR = 88, and low residual heat capacity, $\gamma_{SC} = 23$ mJ mol^{-1} K^{-2}, which leads to entropy conservation. Remarkably, normal state properties such as magnetic susceptibility and Sommerfeld coefficient remain unchanged between superconducting samples. Lattice parameters and site occupancy determined from single-crystal x-ray diffraction also do not change within experimental uncertainty for all superconducting samples investigated here, but a small U deficiency is observed in non-superconducting samples, in agreement with Ref. [31]. Our results suggest that the superconducting state of UTe_2 is sensitive to remarkably subtle structural differences that deserve a central place in future investigations of the intrinsic superconducting properties of UTe_2.

Results

Crystal growth and specific heat. As described in Methods and summarized in Table 1, single crystals of UTe_2 were grown using the chemical vapor transport (CVT) method with iodine as the transport agent. Figure 1a shows the specific heat divided by temperature, C/T, as a function of temperature for seven representative samples. Sample s1 exhibits two well-defined features at $T_{c1} = 1.64$ K and $T_{c2} = 1.48$ K, which is consistent with results from Ref. [26] (group 1) interpreted as distinct superconducting transitions from a multicomponent order parameter. Recent ac calorimetry measurements, however, reveal that T_{c1} and T_{c2} are suppressed at the same rate under hydrostatic pressure, which

Table 1 Crystal growth parameters and physical properties of UTe_2 single crystals.

Sample	T_i (°C)	T_f (°C)	T_c (K)	γ_{SC} (mJ mol^{-1} K^{-2})	RRR $\mu\Omega$ cm	ρ_0	A $\mu\Omega$ cm K^{-2}
s1	1060	1000	1.64(4)/1.48(4)	65	30–40	16	0.5–0.88[14,16,20,39]
s2	950	860	1.68(3)	51	-	-	-
s3	925	835	1.77(3)	43	-	-	-
s4	875	785	1.85(3)	41	55	12	0.97
s5	825	735	1.95(6)	25	70	9	1.03
s6	800	710	2.00(4)	23	88	7	1.00
s7	775	685	N/A	N/A	2	550	N/A

T_i (T_f) is the temperature of the hot (cold) end of the CVT temperature gradient. Importantly, all residual resistivity values (RRR) and residual resistivity values (ρ_0) were calculated for the same configuration, *i.e.*, applied current along the *a* direction.

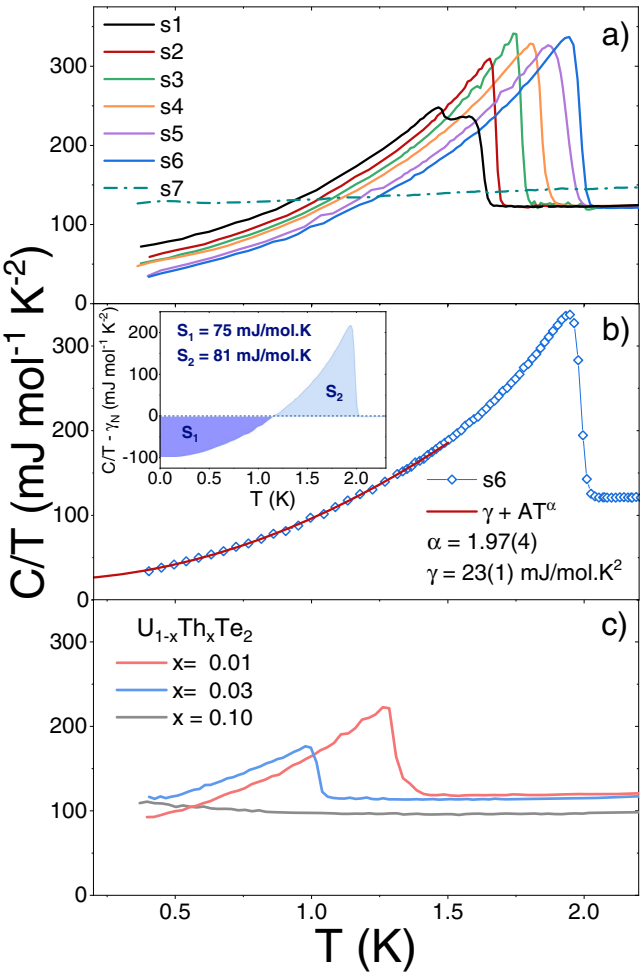

Fig. 1 Specific heat of UTe_2 single crystals. a C/T as a function of temperature for seven representative samples. **b** C/T as a temperature for sample s6. The solid line is a power-law fit below 1.5 K. Inset shows the entropy balance in a $C/T - \gamma_N vs T$ plot. **c** C/T as a function of temperature for Th-doped UTe_2 single crystals.

strongly suggests the presence of two mesoscale regions in the sample (See Erratum in Ref. [21]).

Notably, the double feature at ambient pressure is quickly replaced by a single transition as the growth temperature decreases. Results for samples s2 ($T_c = 1.68$ K) and s3 ($T_c = 1.77$ K) are consistent with reports from group 2[16] and group 3[27], respectively. Here T_c is defined as the midpoint of the rise in C/T on cooling. The optimal superconducting transition temperature is found in sample s6, whose bulk T_c is 2 K. The bulk superconducting transition quickly vanishes in crystals grown at even lower temperatures (sample s7). Importantly, the residual heat capacity value in the superconducting state decreases monotonically as T_c increases. Although changes in the U/Te starting ratio were previously shown to affect T_c[27], our results demonstrate that the optimal T_c in UTe_2 is obtained at lower growth temperatures. We find that slightly larger Te concentrations also quickly suppress T_c. In contrast to variations in T_c and γ_{SC}, the normal state Sommerfeld coefficient is nearly constant for all samples, $\gamma_N = 121(4)$ mJ mol^{-1} K^{-2}.

Figure 1 b shows C/T as a function of temperature for sample s6. At T_c, the magnitude of the superconducting jump divided by the normal state Sommerfeld coefficient is $\Delta C/\gamma_N T_c = 1.8$. This value is larger than the weak coupling BCS limit of 1.43 and agrees with previous results on samples with a single transition higher than 1.7 K[27]. For samples with lower T_c, $\Delta C/\gamma_N T_c$ is smaller and ranges from 1.2 to 1.5[14,16,21,26,28,29]. Notably, a transition temperature of ~2 K has been observed previously in electrical resistivity data, but the associated bulk transition in C/T occurred at lower temperature ~1.77 K[27]. Whether the higher resistive transition is due to surface effects or percolation through filaments in the bulk is still an open question.

The low-temperature C/T behavior of sample s6 can be well described by the power-law expression $\gamma_{SC} + AT^{\alpha}$ wherein $\gamma_{SC} = 23$ mJ mol^{-1} K^{-2} and $\alpha = 1.97(4)$ (solid line in Fig. 1b). The magnitude of the residual Sommerfeld coefficient in the superconducting state of sample s6 is the lowest reported value, which suggests that a larger γ_{SC} value is not an intrinsic property of UTe_2. In addition, the quadratic dependence of C/T indicates the presence of point nodes, in agreement with previous thermal conductivity and specific heat measurements in crystals grown at higher temperatures[27,32,33].

The second-order nature of the superconducting transition in UTe_2 requires entropy to be conserved at T_c. This equality can be probed by comparing the areas enclosed above and below the γ_N baseline. The inset of Fig. 1b shows the difference between C/T and γ_N as a function of temperature as well as the corresponding areas S_1 and S_2. The magnitudes of the two areas differ by less than 8%, in agreement with the expected entropy conservation in UTe_2, whereas samples with lower T_c show an apparent entropy imbalance of about 60%[14,16,21,26]. The remaining small apparent entropy imbalance may be a hint that T_c can still be further improved, though likely not by a significant amount. Alternatively, the imbalance could be tentatively explained by the presence of a nuclear Schottky anomaly at lower temperatures. Finally, we note that a proper phonon subtraction was hindered by the fact that nonmagnetic analog $ThTe_2$ is not known to crystallize in the same strucutre of UTe_2.

To test the solubility of Th in UTe_2, we investigate Th-doped UTe_2 single crystals grown in conditions similar to sample s1, which could also provide access to the unexplored regime of negative chemical pressure in UTe_2. Figure 1c shows the specific heat divided by temperature as a function of temperature for $U_{1-x}Th_xTe_2$ at three Th concentrations. At only 1% Th doping, the superconducting anomaly is substantially suppressed by about 20%. At such low doping, microprobe analysis using energy dispersive x-ray spectroscopy shows that the actual concentration of Th is very close to the nominal concentration, and the doping is fairly homogeneous. For the crystal shown in Fig. 1c, the mean actual concentration is 1.2% and the homogeneity range is about 0.2%. At 3% nominal Th doping, the mean actual concentration is ~4%, but a larger standard deviation of 2% is observed within a crystal. The superconducting transition in specific heat is further suppressed to $T_c = 1$ K at 3% nominal Th doping, whereas no transition is observed at 10% nominal Th doping. Microprobe analysis of the $x = 0.1$ crystal shown in Fig. 1c yields an actual concentration of 24(8)%, but measurements in different crystals from the same batch show significantly different dopings. These results are consistent with an insolubitity region at larger Th concentrations.

Magnetic Susceptibility. Now we turn to the electrical and magnetic properties of sample s5, whose T_c is 1.95 K. Figure 2 shows the anisotropic magnetic susceptibility, $\chi(T)$, of UTe_2 as a function of temperature. Importantly, $\chi(T)$ in the normal state is remarkably similar to previous reports[14,16] and between different samples in this work (see Supplementary Figure S4). The a-axis susceptibility is the largest, which suggests that the a axis is the easy axis. The c-axis susceptibility is small and monotonic, whereas the b-axis susceptibility shows a broad feature centered

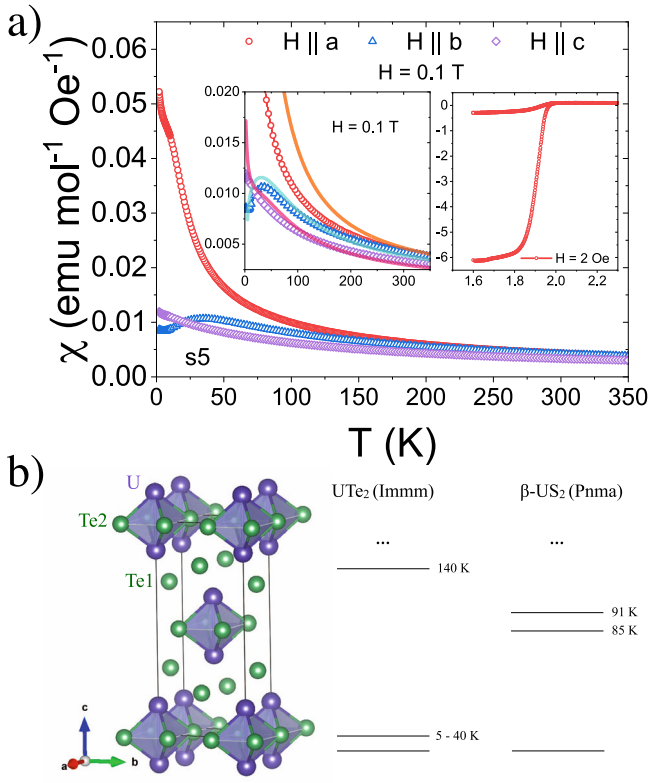

Fig. 2 Magnetic properties and CEF levels in UTe_2. a Anisotropic magnetic susceptibility of UTe_2 as a function of temperature at 0.1 T. Right inset shows the zero-field-cooled and field-cooled magnetic susceptibility at 2 Oe with field applied along the *a* axis. Left inset shows the high-temperature anisotropic magnetic susceptibility and the associated crystal electric field fits (solid lines). **b** (Left) Crystal structure of UTe_2 highlighting the polyhedra enclosing the *c*-axis uranium-uranium dimer. (Right) Comparison of crystal electric field levels of UTe_2 and β-US_2.

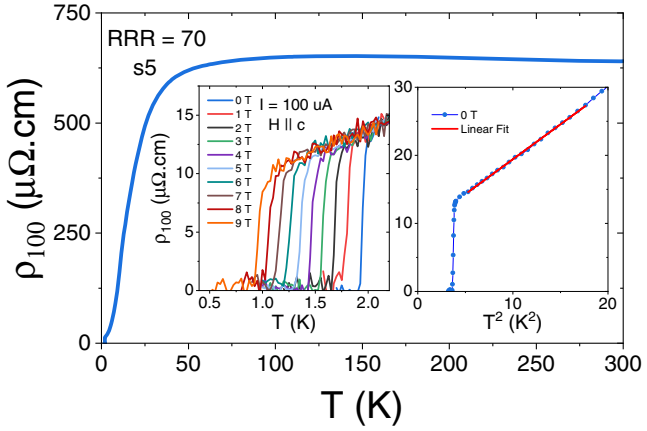

Fig. 3 Electrical resistivity of UTe_2. Electrical resistivity of UTe_2 (sample s5) as a function of temperature with current along the *a* axis. Inset shows the low-temperature behavior under magnetic fields applied along *c*.

at ~35 K. The right inset of Fig. 2 displays the zero-field-cooled and field-cooled $\chi(T)$ at 2 Oe with field applied along the *a* axis. A clear diamagnetic signal sets in at 1.95 K, which is consistent with electrical resistivity and specific heat data. No evidence for impurity phases is found at low fields (see Supplementary Figure S5).

Crystal electric field (CEF) effects are able to capture the qualitative $\chi(T)$ behavior of UTe_2. The solid lines in the left inset of Figure 2 show fits of the data to an orthorhombic CEF Hamiltonian $\mathcal{H}_{\mathrm{CEF}} = B_2^0O_2^0 + B_2^2O_2^2 + B_4^0O_4^0 + B_4^2O_4^2 + B_4^4O_4^4$, where B_i^n are the CEF parameters, and O_i^n are the Stevens equivalent operators obtained from the angular momentum operators[34]. Here we consider the $5f^2$ configuration of uranium, i.e., U^{4+} ($J = 4$, $S = 1$), as the localized configuration that gives rise to CEF effects. This consideration is based on three experimental results. First, x-ray absorption measurements under pressure suggest that UTe_2 is mixed valence at ambient pressure and goes towards $4+$ when magnetic order sets in under pressure[21]. Second, core-level spectroscopy measurements also argue for a mixed-valence configuration wherein the dominant contribution arises from the itinerant $5f^3$ configuration and a smaller localized $5f^2$ contribution is responsible for a satellite peak[35]. Third, angle-resolved photoemission spectroscopy measurements combined with DFT+DMFT (density functional theory + dynamical mean-field theory) calculations find two $5f^2$ atomic multiplet configurations centered around 0.7 eV binding energy[36]. Finally, a $5f^3$ configuration for uranium did not provide reasonable CEF fits to the data.

The orthorhombic crystalline environment splits the 9-fold degenerate multiplet of $J = 4$ U^{4+} into a collection of singlets. The relevant levels below room temperature are described by a combination of two low-lying singlets and an excited singlet at 140 K. As shown in Figure 2b, this configuration resembles that of β-US_2, whose experimentally-determined crystal field levels are given by a ground state singlet separated by 85 K and 91 K from two excited singlets. Akin to UTe_2, β-US_2 also orders magnetically under pressure, which indicates that the admixture of three low-lying singlets yields a finite magnetic moment. In fact, the ground state and the second excited state at 140 K in UTe_2 form a quasi-doublet, i.e., they share the same $|j_z\rangle$ contributions $|\pm 4\rangle$, $|\pm 2\rangle$, and $|0\rangle$. The CEF parameters and corresponding energy levels and wavefunctions are shown in Supplementary Table S1.

Electrical Resistivity. Figure 3 shows the electrical resistivity with applied current along the *a* axis, ρ_{100}, as a function of temperature for sample s5. At high temperatures, ρ_{100} increases slightly on cooling, which is consistent with previous reports and stems from incoherent Kondo scattering. At about 40 K, ρ_{100} decreases sharply on cooling, a behavior typically attributed to the formation of a Kondo coherent state. This coherence temperature is also consistent with estimates from scanning tunneling microscopy[37].

The inset of Fig. 3 shows the low-temperature behavior of ρ_{100} at various magnetic fields applied along the *c* axis. At zero field, the mid-point of the superconducting transition is at 1.95 K, which is precisely the value obtained from specific heat measurements. At 9 T, T_c is reduced to 1 K, which is consistent with previous reports by taking into account a 0.3 K shift in the zero-field T_c[14,16]. The modified phase diagrams, however, do not overlap perfectly as shown in Supplementary Figure S6. Though this mismatch might suggest the presence of a small field-dependent shift, we cannot rule out small differences in experimental conditions between different groups at this moment. Finally, the residual resistivity ratio (RRR), defined as $[\rho(300\,K) - \rho(T = 0))/\rho(T = 0)]$, is 70, which is the highest reported value for ρ_{100}. In contrast, the RRR value of non-superconducting sample s7 is only 2 (see Table 1). The residual resistivity, $\rho(T = 0) = \rho_0$, was obtained by a low-temperature fit to $\rho_0 + AT^2$ as shown in the right inset of Fig 3, akin to the procedure performed as a function of magnetic field in Ref. [38]. To our knowledge, $\rho_0 = 7\mu\Omega$ cm of sample s6 is the lowest reported value for UTe_2 (see Supplementary Figure S7). Finally, we note that a modest increase in the Fermi-liquid *A* coefficient appears to

be present in samples s4-s6 compared to samples grown at higher temperatures, which may suggest a small increase in correlations, i.e., effective mass[14,16,20,39].

Discussion

Both ρ_0 and RRR values are commonly used criteria for the presence of disorder and have been successfully utilized to infer the quality of unconventional superconductors, including UTe_2 by groups 1 and 2[16,26]. The pressing question therefore relates to the cause of the underlying disorder in UTe_2. Historically, planar defects, grain boundaries, and substitutional or interstitial impurities have been argued to affect the sample quality of various actinide superconductors, including UPt_3[40], UBe_{13}[41], UCoGe[42], and URu_2Si_2[43]. More broadly, disorder has been shown to reduce T_c in other unconventional superconductors such as Sr_2RuO_4[44] and FeSe[45]. Recent reports have argued that Te vacancies are responsible for lower superconducting transitions in UTe_2[27]. Remarkably, in the present study we do not observe statistically relevant differences in microprobe analysis through energy-dispersive x-ray spectroscopy. All superconducting single crystals investigated here showed a stoichiometry of $UTe_{2.2(3)}$, i.e., the large error bars hinder the establishment of any possible trends. This result is supported by standard laboratory single crystal x-ray diffraction of samples s1, s4, and s6, wherein both uranium and tellurium sites are fully occupied. Notably, a small U deficiency is observed in non-superconducting samples, in agreement with Ref. [31]. In addition, lattice parameters as well as all refined parameters are constant across all superconducting samples investigated here within experimental uncertainty. Supplementary Tables S2–S3 and Figs. S1–S3 provide details of the full refinements. Notably, the anisotropic atomic displacement parameters U^{11} (displacement along the a direction) and U^{22} (displacement along the b direction) do not change as a function of T_c within the experimental uncertainty; however, there is an apparent trend for U^{33} (displacement along the c direction), namely, samples with larger T_c tend to exhibit smaller U^{33} (Supplementary Fig. S3). This trend would be consistent with the key role of the uranium-uranium dimer interaction in the superconducting state of UTe_2. The significant spread within samples, however, prevents a more definitive statement at the current stage. In addition, the reported evidence for spatial inhomogeneity in double-transition samples further highlights the need for additional structural measurements to probe the presence of multiple phases in the mesoscale[28]. Our results suggest that the superconducting state of UTe_2 is remarkably sensitive to disorder and calls attention to the importance of determining the main structural parameter that suppresses and splits T_c.

Conclusions

In summary, we report the optimal superconducting transition temperature, $T_c = 2$K, in UTe_2 single crystals. Our crystals exhibit a single superconducting transition and their high quality is demonstrated by high residual resistance ratios, RRR = 88, and low residual heat capacity values in the superconducting state, $\gamma_{SC} = 23$ mJ mol^{-1} K^{-2}, which leads to the expected entropy conservation. The correlation between T_c and residual resistance ratios underscores the role of disorder in the superconducting state of UTe_2. The disappearance of the double transition feature as sample quality is improved brings into question whether UTe_2 is a multi-component superconductor at ambient pressure.

Methods

Crystal Growth. Single crystals of UTe_2 were grown using the chemical vapor transport method. Solid pieces of depleted uranium (99.99%) and tellurium (Alfa Aesar, 99.9999 + %) were weighed in a 2:3 ratio with total mass of ~1 g. The elements were sealed under vacuum using a hydrogen torch in a quartz tube along with ~0.2 g of iodine (Alfa Aesar, 99.99 + %). The dimensions of the quartz tube are 1.8 cm (outer diameter), 1.4 cm (inner diameter), and ~15 cm (length), which resulted in an iodine density of about 0.8 mg cm^{-3}. A temperature gradient was maintained in a multi-zone furnace for 11 days. The elements were placed in the hot end of the gradient at T_i, whereas single crystals of UTe_2 were obtained at T_f, the cold end of the gradient. T_i was varied from 1060 °C to 800 °C, whereas T_f was varied from 1000 °C to 710 °C. A summary of the growth conditions of representative samples is presented in Table 1. In our nomenclature, any sample grown in a temperature gradient between 1060 °C and 1000 °C will contain number "1" in their label. For Th-doped samples, Th and U were arc melted in a water-cooled Cu hearth prior to the growth.

Structural analysis. The crystallographic structure of UTe_2 was determined at room temperature by a Bruker D8 Venture single-crystal diffractometer equipped with Mo radiation. In Supplementary Information Note 2, several crystals were investigated from batches grown under the same conditions as sample s1 in the main text. The single crystal labeled s1 in the main text was cut into four pieces, and the heat capacity of each piece was measured in Ref. [28], Fig 2b. Samples R2, R3, and R4 in Ref. [28] correspond to S1 B, C, and D in this work, respectively. Samples 1E and 1F were grown following the same synthetic conditions as Samples 1B-D, but Sample 1F only has one specific heat transition.

Elemental analysis of our single crystals was performed using energy-dispersive x-ray spectroscopy in a commercial scanning electron microscope.

Sample storage. Single crystals of UTe_2 are sensitive to air and moisture, and they were kept in an argon glovebox between measurements to allow for sample stability over several months.

Electrical transport and thermodynamic measurements. Magnetization measurements were obtained through a commercial SQUID-based magnetometer. Specific heat measurements were made using a commercial calorimeter that utilizes a quasi-adiabatic thermal relaxation technique. The electrical resistivity (ρ) was characterized using a standard four-probe configuration with an AC resistance bridge. Values of RRR in Table I were determined for current flow along the a axis.

Data availability

CSD 2132551-2132559 contains part of the supplementary crystallographic data for this paper. Sample 1B, C, D, E, and F are represented by 2132554, 2132555, 2132556, 2132553, 2132552, respectively. Sample 4 is represented by 2132557. Sample 6A and 6B are represented by 2132551 and 2132558, respectively. Sample 7B is represented by 2132559. The data can be obtained free of charge from The Cambridge Crystallographic Data Centre via http://www.ccdc.cam.ac.uk/structures. All other data is available from the corresponding author upon reasonable request.

Received: 25 October 2021; Accepted: 22 April 2022;
Published online: 23 May 2022

References

1. Hill, H. H. Plutonium 1970 and Other Actinides. In Miner, W. N. (ed.) *Plutonium 1970 Other Actinides* (The Metallurgical Society of the AIME, 1970).
2. Moore, K. T. & Van Der Laan, G. Nature of the 5f states in actinide metals. *Revi. Modern Phys.* **81**, 235–298 (2009).
3. Palstra, T. T. M. et al. Superconducting and Magnetic Transitions in the Heavy-Fermion System URu2Si2. *Phys. Rev. Lett.* **55**, 2727–2730 (1985).
4. Mydosh, J. A. & Oppeneer, P. M. Colloquium : Hidden order, superconductivity, and magnetism: The unsolved case of URu2Si2. *Rev. Modern Phys.* **83**, 1301–1322 (2011).
5. Schemm, E. R., Gannon, W. J., Wishne, C. M., Halperin, W. P. & Kapitulnik, A. Observation of broken time-reversal symmetry in the heavy-fermion superconductor UPt3. *Science* **345**, 190–193 (2014).
6. Avers, K. E. et al. Broken time-reversal symmetry in the topological superconductor UPt3. *Nat. Phys.* **16**, 531–535 (2020).
7. Han, S. et al. Observation of Negative s-Wave Proximity Effect in Superconducting UBe13. *Phys. Rev. Lett.* **57**, 238–241 (1986).
8. Shimizu, Y. et al. Field-Orientation Dependence of Low-Energy Quasiparticle Excitations in the Heavy-Electron Superconductor UBe13. *Phys. Rev. Lett.* **114**, 147002 (2015).
9. Shimizu, Y., Braithwaite, D., Aoki, D., Salce, B. & Brison, J.-P. Spin-triplet p-wave superconductivity revealed under high pressure in ube13. *Phys. Rev. Lett.* **122**, 067001 (2019).
10. Geibel, C. et al. Heavy-fermion superconductivity at Tc=2K in the antiferromagnet UPd2Al3. *Zeitschrift fur Phys. B Condens. Matter* **84**, 1–2 (1991).

11. Pfleiderer, C. Superconducting phases of f-electron compounds. *Rev. Modern Phys.* **81**, 1551–1624 (2009).
12. Saxena, S. S. et al. Superconductivity on the border of itinerant-electron ferromagnetism in UGe2. *Nature* **406**, 587–592 (2000).
13. Aoki, D., Ishida, K. & Flouquet, J. Review of U-based Ferromagnetic Superconductors: Comparison between UGe 2, URhGe, and UCoGe. *J. Phys. Soc. Japan* **88**, 022001 (2019).
14. Ran, S. et al. Nearly ferromagnetic spin-triplet superconductivity. *Science* **365**, 684–687 (2019).
15. Ran, S. et al. Extreme magnetic field-boosted superconductivity. *Nat. Phys.* **15**, 1250–1254 (2019).
16. Aoki, D. et al. Unconventional Superconductivity in Heavy Fermion UTe2. *J. Phys. Soc. Japan* **88**, 043702 (2019).
17. Knebel, G. et al. Field-Reentrant Superconductivity Close to a Metamagnetic Transition in the Heavy-Fermion Superconductor UTe2. *J. Phys. Soc. Japan* **88**, 063707 (2019).
18. Nakamine, G. et al. Superconducting Properties of Heavy Fermion UTe2 Revealed by 125 Te-nuclear Magnetic Resonance. *J. Phys. Soc. Japan* **88**, 113703 (2019).
19. Sundar, S. et al. Coexistence of ferromagnetic fluctuations and superconductivity in the actinide superconductor UTe2. *Phys. Rev. B* **100**, 140502 (2019).
20. Braithwaite, D. et al. Multiple superconducting phases in a nearly ferromagnetic system. *Commun. Phys.* **2**, 147 (2019).
21. Thomas, S. M. et al. Evidence for a pressure-induced antiferromagnetic quantum critical point in intermediate-valence UTe 2. *Sci. Adv.* **6**, eabc8709 (2020).
22. Li, D. et al. Magnetic Properties under Pressure in Novel Spin-Triplet Superconductor UTe2. *J. Phys. Soc. Japan* **90**, 073703 (2021).
23. Duan, C. et al. Incommensurate Spin Fluctuations in the Spin-Triplet Superconductor Candidate UTe2. *Phys. Rev. Lett.* **125**, 237003 (2020).
24. Duan, C. et al. Resonance from antiferromagnetic spin fluctuations for spin-triplet superconductivity in UTe2. *Nature***600**, 636–640 (2021).
25. Knafo, W. et al. Low-dimensional antiferromagnetic fluctuations in the heavy-fermion paramagnetic ladder UTe2. *Phys. Rev. B* **104**, L100409 (2021).
26. Hayes, I. M. et al. Multicomponent superconducting order parameter in UTe 2. *Science* **373**, 797–801 (2021).
27. Cairns, L. P., Stevens, C. R., O'Neill, C. D. & Huxley, A. Composition dependence of the superconducting properties of UTe 2. *J. Phys. Condens. Matter* **32**, 415602 (2020).
28. Thomas, S. M. et al. Spatially inhomogeneous superconductivity in UTe2. *Phys. Rev.B* **104**, 224501 (2021).
29. Aoki, D. et al. Unconventional superconductivity in ute2. *J. Phys. Condens. Matter* **34**, 243002 (2022).
30. Aoki, D. et al. Multiple Superconducting Phases and Unusual Enhancement of the Upper Critical Field in UTe2. *J. Phys. Soc. Japan* **89**, 053705 (2020).
31. Haga, Y. et al. Effect of uranium deficiency on normal and superconducting properties in unconventional superconductor ute2. *J. Phys. Condens. Matter* **34**, 175601 (2022).
32. Metz, T. et al. Point-node gap structure of the spin-triplet superconductor UTe2. *Phys. Rev. B* **100**, 220504 (2019).
33. Kittaka, S. et al. Orientation of point nodes and nonunitary triplet pairing tuned by the easy-axis magnetization in UTe2. *Phys. Rev. Res.* **2**, 032014 (2020).
34. Pagliuso, P. G. et al. Evolution of the magnetic properties and magnetic structures along the RmMIn3m+2 (R=Ce, Nd, Gd, Tb; M=Rh, Ir; and m=1,2) series of intermetallic compounds. *J. Appl. Phys.* **99**, 08P703 (2006).
35. ichi Fujimori, S. et al. Core-level photoelectron spectroscopy study of ute2. *J. Phys. Soc. Japan* **90**, 015002 (2021).
36. Miao, L. et al. Low energy band structure and symmetries of ute2 from angle-resolved photoemission spectroscopy. *Phys. Rev Lett.* **124**, 076401 (2020).
37. Jiao, L. et al. Chiral superconductivity in heavy-fermion metal UTe2. *Nature* **579**, 523–527 (2020).
38. Knafo, W. et al. Comparison of two superconducting phases induced by a magnetic field in ute2. *Commun. Phys.* **4**, 40 (2021).
39. Eo, Y. S. et al. Anomalous c-axis transport response of ute2 (2021). 2101.03102.
40. Kycia, J. B. et al. Suppression of superconductivity in upt3 single crystals. *Phys. Rev. B* **58**, R603–R606 (1998).
41. Amon, A. et al. Tracking aluminium impurities in single crystals of the heavy-fermion superconductor ube13. *Sci. Rep.* **8**, 10654 (2018).
42. Huy, N., Huang, Y. & de Visser, A. Effect of annealing on the magnetic and superconducting properties of single-crystalline ucoge. *J. Magnet. Magnetic Mat.* **321**, 2691–2693 (2009).
43. Gallagher, A. et al. Single crystal growth of uru2si2 by the modified bridgman technique. *Crystals* **6**, 128 (2016).
44. Mackenzie, A. P. et al. Extremely strong dependence of superconductivity on disorder in sr2ruo4. *Phys. Rev. Lett.* **80**, 161–164 (1998).
45. Böhmer, A. E., Taufour, V., Straszheim, W. E., Wolf, T. & Canfield, P. C. Variation of transition temperatures and residual resistivity ratio in vapor-grown fese. *Phys. Rev. B* **94**, 024526 (2016).

Acknowledgements

We would like to acknowledge constructive discussions with M Bordelon, YS Eo, N Butch, JP Paglione, A Huxley, and RM Fernandes. This material is based upon work supported by the U.S. Department of Energy, Office of Science, National Quantum Information Science Research Centers, Quantum Science Center. Scanning electron microscope and energy dispersive x-ray measurements were supported by the Center for Integrated Nanotechnologies, an Office of Science User Facility operated for the U.S. Department of Energy Office of Science. AW acknowledges support from the Laboratory Directed Research and Development program at LANL.

Author contributions

P.F.S.R. grew the samples, performed the elemental analysis, and performed the crystaline electric field fits. P.F.S.R. and S.M.T. performed the electrical resistivity and specific heat measurements. A.W., S.S.F., and B.L.S. performed the x-ray diffraction measurements. J.D.T performed the magnetic susceptibility measurements. E.D.B. and F.R. participated in discussions and data analyses. All authors participated in the interpretation of the data and the writing of the manuscript.

Competing interests

The authors declare no competing interests.

Additional information

Supplementary information The online version contains supplementary material available at https://doi.org/10.1038/s43246-022-00254-2.

Correspondence and requests for materials should be addressed to Priscila F. S. Rosa.

Peer review information *Communications Materials* thanks the anonymous reviewers for their contribution to the peer review of this work. Primary Handling Editors: Nicola Poccia and Aldo Isidori.

Reprints and permission information is available at http://www.nature.com/reprints

Publisher's note Springer Nature remains neutral with regard to jurisdictional claims in published maps and institutional affiliations.